

The recirculation flow after different cross-section shaped high-rise buildings with applications to ventilation assessment and drag parameterization

Keyi Chen^{1,2}, Ziwei Mo^{1,2} (✉), Jian Hang^{1,2}

1. School of Atmospheric Sciences, Sun Yat-sen University & Southern Marine Science and Engineering Guangdong Laboratory, Zhuhai 519082, China

2. Key Laboratory of Tropical Atmosphere-Ocean System, Ministry of Education, Zhuhai 519000, China

Abstract

The building cross-section shape significantly affects the flow characteristics around buildings, especially the recirculation region behind the high-rise building. Eight generic building shapes including square, triangle, octagon, T-shaped, cross-shaped, #-shaped, H-shaped and L-shaped are examined to elucidate their effects on the flow patterns, recirculation length L and areas A using computational fluid dynamics (CFD) simulations with Reynolds-averaged Navier-Stokes (RANS) approach. The sizes and positions of the vortexes behind the buildings are found to be substantially affected by the building shapes and subsequently changing the recirculation flows. The recirculation length L is in the range of $1.6b - 2.6b$ with an average of $2b$. The maximum L is found for L-shaped building ($2.6b$) while the shortest behind octagon building ($1.6b$). The vertical recirculation area A_v is in the range of $1.5b^2 - 3.2b^2$ and horizontal area A_h in $0.9b^2 - 2.2b^2$. The L , A_v and A_h generally increase with increasing approaching frontal area when the wind direction changes but subject to the dent structures of the #-shaped and cross-shaped buildings. The area-averaged wind velocity ratio (AVR), which is proposed to assess the ventilation performance, is in the range of 0.05 and 0.14, which is around a three-fold difference among the different building shapes. The drag coefficient parameterized by A_h varies significantly, suggesting that previous models without accounting for building shape effect could result in large uncertainty in the drag predictions. These findings provide important reference for improving pedestrian wind environment and shed some light on refining the urban canopy parameterization by considering the building shape effect.

1 Introduction

During the process of urban development and expansion, the building density, size and geometry are changing dramatically, especially in the megacities such as Guangdong-Hong Kong-Macao Greater Bay Area (GBA), China. Buildings can block the atmospheric flow, altering the wind direction and velocity, which in turns significantly affect the pedestrian level wind comfort in the building surroundings (Du and Mak 2017; Serteser and Karadag 2018; Li and Chen 2020). To satisfy the needs of urban residents in high-level living standards, more comfortable and safer

wind environment are required in the high dense cities. Therefore, advanced understandings of the urban wind flow are utmost important in building a healthy and sustainable urban environment.

Computational fluid dynamics (CFD) technique has been widely adopted in simulating the flow field in the vicinity of buildings and atmospheric boundary layer, which assists in evaluating the pedestrian wind comfort, wind loads on buildings, and pollutant dispersion (Tominaga and Stathopoulos 2013; Blocken et al. 2016; Thordal et al. 2019). CFD modeling of flows around a simplified, square-shaped high-rise buildings provides basic understandings of the

Keywords

recirculation region
cross-section shape
ventilation assessment
drag parameterization
computational fluid dynamics

Article History

Received: 24 August 2023

Revised: 25 November 2023

Accepted: 11 December 2023

© Tsinghua University Press 2024

List of symbols

A	recirculation area	R	speed-up ratio
A_f	frontal area of the buildings	R^2	determination of coefficient
A_h	horizontal recirculation area	RMSE	root mean square error
A_p	building floor area	U	mean wind velocity
A_t	total floor area	U_{avg}	area-averaged wind velocity
A_v	vertical recirculation area	U_i	mean wind velocity at point i with the building
AVR	area-averaged wind velocity ratio	U_{i0}	mean wind velocity at point i without the building
b	width (m)	U_{ref}	reference wind speed
C_1	curve-fitting coefficient	u^*	friction velocity
$C_{1\epsilon}$	modelling constant	\bar{u}_i	mean velocity
C_2	curve-fitting coefficient	VR	wind velocity ratio
$C_{2\epsilon}$	modelling constant	x_i	instantaneous position
C_d	drag coefficient	z	height coordinate
C_R	drag constant for an isolated, surface-mounted roughness element	z_0	aerodynamic roughness length
C_μ	empirical modelling constant	z_{ref}	reference height
d	ground-normal displacement height	δ_{ij}	Kronecker delta
h	height (m)	ϵ	TKE dissipation rate
k	turbulent kinematic energy (TKE)	κ	von Karman constant
l	length (m)	λ_f	frontal area index
L	recirculation length	λ_p	planar area index
MVR	mean wind velocity ratio	ν_t	turbulent viscosity
P_k	TKE production	σ_k	Prandtl number
\bar{p}	kinematic pressure	σ_ϵ	Prandtl number

flow patterns and structures in urban areas. Different turbulence models of steady and unsteady Reynolds averaged Navier-Stokes (RANS) were used to evaluate the flow fields around an isolated building with the size of building length l : width b : height $h = 1:1:2$ (Tominaga 2015). Large eddy simulation (LES) and detached eddy simulation (DES) were also assessed and compared with the wind tunnel measurement (Liu and Niu 2016). In view of the complicated structure of three-dimensional turbulence behind the high-rise building, recent studies advanced statistical technique—spectral proper orthogonal decomposition (SPOD) to elucidate the turbulent structures (Zhang et al. 2020a, 2021). These studies greatly advance our understandings of the flow patterns around the 1:1:2 building. CFD modeling of a single high-rise building can also be used to develop the drag model to improve the urban canopy parameterizations (Shao and Yang 2005; Santiago and Martilli 2010; Fan et al. 2022).

Modern design and architectural techniques foster more complex buildings in shapes and forms. The impacts of building structures, such as roof and balcony, on the flow field and pollutant dispersion were studied intensively in recent years (Tominaga et al. 2015; Hemida et al. 2020;

Zheng et al. 2020; Liu et al. 2021; Vranešević et al. 2022). Some studies also focused on the influence of side ratio on wind environment and pollutant dispersion (Kono et al. 2016; Jiang and Yoshie 2020). In particular, the building cross-section shape (hereafter specified as building shape) is an important factor that could influence the flow structures and wake regions. Lee and Mak (2022) compared the wind flow characteristics and ventilation performance around the “+”-shaped and “T”-shaped buildings under different approaching wind directions using RANS modeling. In the wake of “T”-shaped building, compared with the incident wind direction 0° , the downwind length and maximum bilateral width of the low-wind velocity region reduced respectively by 11.5% and 37.9% when the wind angle was 90° . Chen and Mak (2021) further discussed the pedestrian-level wind comfort around 22 different buildings (e.g. polygonal, slab-like, cruciform) with lift-up design. It is suggested that the lift-up design is conducive to improving the pedestrian level wind comfort around the buildings but subjected to different incident wind directions and building configurations. The pollutant dispersions were also highly modified by building shapes (including chamfered, square, circular, and curved) revealed by the LES study (Keshavarzian

et al. 2021). The pollutant emission regions were enlarged behind the chamfered and square buildings. The wind fields around the super tall building-skyscraper were also studied with application to wind environment assessment at pedestrian level (Yang et al. 2022). The wind speed ratio was used to evaluate the pedestrian-level wind environment under various incident wind directions around the super-tall buildings with tapered, helical, triangular and polygonal shapes (Xu et al. 2017; Tamura et al. 2017; Zhang et al. 2020b; c). In addition to the airflow (Korycki et al. 2016) and pollutant dispersion (Yu et al. 2017), additional studies evaluated the aerodynamic effect and wind loads on the high-rise buildings with different cross-section shapes (Kasana et al. 2022; Meena et al. 2022; Rukhaiyar et al. 2023).

Although the above-mentioned studies provide important references for understanding the effects of building shapes with the focus on different aspects, such as flow structure, pedestrian wind environment, wind load, and pollutant dispersion. Besides, they focus on only several generic shapes including square, circular and cross (Keshavarzian et al. 2021; Lee and Mak 2022) and a few specific ones, such as polygonal, tapered and helical (Xu et al. 2017; Tamura et al. 2017). There are still insufficient researches on the buildings with different generic shapes. The lack of comprehensive understandings of flow structures, vortex locations, flow recirculation sizes behind the buildings limited the ventilation and wind comfort assessment as well as accurate parameterizations of the aerodynamic effect in urban areas. In particular, the length and area of the recirculation area still need to be studied under the condition of different building shapes, heights and wind directions, which will

contribute to the evaluation of wind environment and the parameterization of drag coefficient in the urban canopy model.

In this study, the CFD-RANS model is used to simulate the wind fields around an isolated high-rise building of eight generic shapes. By varying the building cross-section shapes, building heights and wind directions, this study aims to examine their effects on the (1) flow and vortex characteristics, (2) recirculation length and area, (3) ventilation and wind comfort behind an isolated high-rise building and (4) the parameterization of drag coefficient C_d . The findings of this study will benefit the quantitative assessment of urban ventilation and pedestrian-level wind environment, canopy model development, as well as urban climate design and sustainable environment development.

2 Methodology

2.1 Simulation cases

Eight building shapes commonly found in the highly urbanized city cluster of China: Guangdong-Hong Kong-Macao Greater Bay Area (GBA) are selected in this study. The satellite images and simplified models are shown in Figure 1, including “Square”, “Triangle”, “Octagon”, “T-shaped”, “Cross-shaped”, “#-shaped”, “H-shaped” and “L-shaped”. The building-height-to-width (aspect) ratios $h:b$ of each building model is $h:b = 60m:30m = 2:1$. We take the simplified 2:1 square model as the base case and change the building shape to investigate the influence on the recirculation flow. All of these models have the same windward area at the approaching

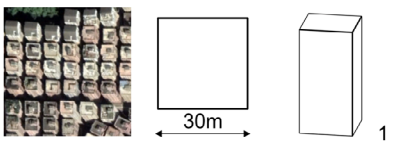
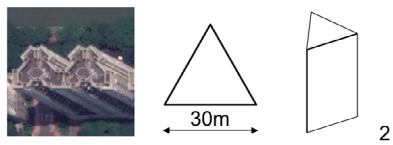
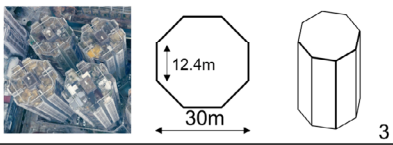
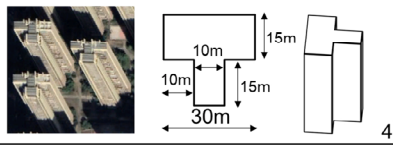
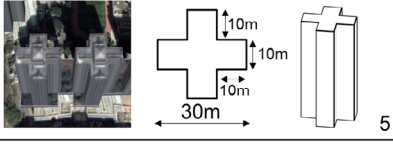
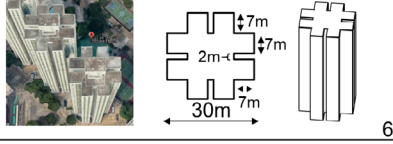
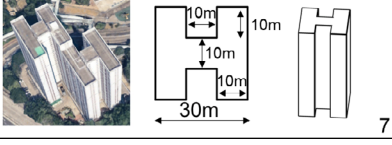
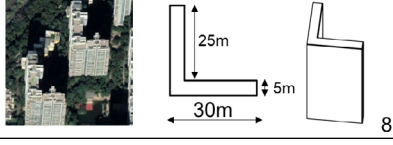
Square		Triangle	
Octagon		T-shaped	
Cross-shaped		#-shaped	
H-shaped		L-shaped	

Fig. 1 The satellite images (retrieved from google earth) of buildings with different cross-section shapes and their simplified models considered in this study

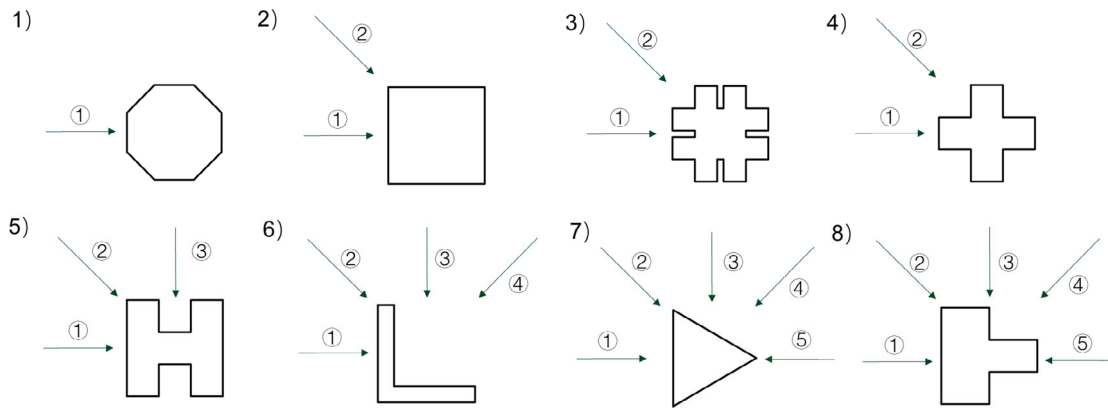


Fig. 2 The schematics of the incident wind directions for different building shapes: ① approaching wind $\theta = 0^\circ$; ② oblique approaching wind $\theta = 45^\circ$; ③ lateral approaching wind $\theta = 90^\circ$; ④ Oblique opposing wind $\theta = 135^\circ$; ⑤ Opposing wind $\theta = 180^\circ$

wind $\theta = 0^\circ$. In order to explore the influence of different incident wind directions on recirculation flow behind the buildings, this study also sets simulation cases of different wind directions for buildings with various shapes as detailed in Figure 2. The octagon model case only covers 0° . The square, #-shaped and cross-shaped model cases cover 0° and 45° . The H-shaped model case covers 0° , 45° , 90° . The L-shaped model case covers 0° , 45° , 90° , 135° . The triangle and T-shaped model cases cover 0° , 45° , 90° , 135° , 180° . Furthermore, the square models with building-height-to-width (aspect) ratios $h:b = 3:1$ and $4:1$ are also considered to investigate the impact of the building height. As tabulated in Table 1, a total of 26 cases are tested to examine the effect of the building shape, height and the wind direction on the wind flow in the recirculation region after the high-rise building.

2.2 RANS model

The RANS turbulence model is used because of the

Table 1 The building shapes, building-height-to-width (aspect) ratios ($h:b$), wind directions, and number of simulation cases

Cases	$h:b$	Wind directions	No. of Cases
Square (base case)	2:1	0°	1
	2:1	45°	1
Square	3:1	0°	1
	4:1	0°	1
Triangle	2:1	0° 45° 90° 135° 180°	5
Octagon	2:1	0°	1
T-shaped	2:1	0° 45° 90° 135° 180°	5
Cross-shaped	2:1	0° 45°	2
#-shaped	2:1	0° 45°	2
H-shaped	2:1	0° 45° 90°	3
L-shaped	2:1	0° 45° 90° 135°	4
Total No. of cases			26

computational efficient and the excellent simulation of flow patterns around buildings. Although previous studies show that LES can give instantaneous information about turbulence and it is considered more accurate, it takes much more computational cost than RANS model (Tominaga and Stathopoulos 2011; Yu et al. 2017). RANS model is a relatively reliable and effective model for understanding the average wind velocity and flow pattern in the recirculation area and comparing the influences of different building configurations. The $k-\varepsilon$ model is the most commonly used RANS model.

The governing equations for steady-state incompressible, isothermal flows include the continuity equation

$$\frac{\partial \bar{u}_i}{\partial x_i} = 0 \quad (1)$$

and the momentum conservation equation

$$\bar{u}_j \frac{\partial \bar{u}_i}{\partial x_j} = -\frac{\partial \bar{p}}{\partial x_i} - \frac{\partial}{\partial x_j} \overline{u'_i u'_j} \quad (2)$$

where \bar{u}_i is the mean velocity, x_i is the instantaneous position (streamwise x and vertical z direction), \bar{p} is the kinematic pressure. The overbars and primes denote mean and turbulent quantities, respectively.

The Reynolds stresses are approximated by the eddy viscosity and Boussinesq assumption

$$-\overline{u'_i u'_j} = \nu_t \left(\frac{\partial \bar{u}_i}{\partial x_j} + \frac{\partial \bar{u}_j}{\partial x_i} \right) - \frac{2}{3} \delta_{ij} k \quad (3)$$

where $k (= \overline{u'_i u'_i} / 2)$ is the turbulent kinematic energy (TKE), $\nu_t (= C_\mu k^2 / \varepsilon)$ the turbulent viscosity, $C_\mu (= 0.09)$ an empirical modelling constant and δ_{ij} the Kronecker delta. The transport equation for k is

$$\bar{u}_i \frac{\partial k}{\partial x_i} = \frac{\partial}{\partial x_i} \left[\left(\nu + \frac{\nu_t}{\sigma_k} \right) \frac{\partial k}{\partial x_i} \right] + P_k - \varepsilon \quad (4)$$

and the TKE dissipation rate ε is

$$\bar{u}_i \frac{\partial \varepsilon}{\partial x_i} = \frac{\partial}{\partial x_i} \left[\left(\nu + \frac{\nu_t}{\sigma_\varepsilon} \right) \frac{\partial \varepsilon}{\partial x_i} \right] + C_{1\varepsilon} \frac{\varepsilon}{k} P_k - C_{2\varepsilon} \frac{\varepsilon^2}{k} \quad (5)$$

where, $\sigma_k (=1.00)$ and $\sigma_\varepsilon (=1.30)$ are the Prandtl numbers, $C_{1\varepsilon} (=1.44)$, and $C_{2\varepsilon} (=1.92)$ are modelling constants, and $P_k (= \nu_t (\partial \bar{u}_i / \partial x_j + \partial \bar{u}_j / \partial x_i) \times (\partial \bar{u}_i / \partial x_j))$ is TKE production.

2.3 Computational settings

As shown in Figure 3, the computational domain size is length \times width \times height = $21b \times 13b \times 10b$. The similar setting has been adopted in previous RANS and LES studies (Liu and Niu 2016; Zhang et al. 2020a, 2021; Ding et al. 2022), suggesting that the domain size is sufficient large enough to characterize the mean flow and turbulence around the 2:1 square model. The distances from the building model to the inlet boundary, lateral boundaries, top boundary and outlet boundary are $5b$, $6b$, $8b$ and $15b$, respectively. We also carried out the simulation using the expanded domain with $5H$ from the building to the top, sides and upstream domain boundary and $15H$ from the building to downstream domain boundary, which recommended by the AIJ guideline. The mean wind speed profiles for two computational domains show a good agreement with determination of coefficient R^2 over 99% and root mean square error RMSE less than 0.02, supporting the reliability and model performance using a small domain in order to increase the computational efficiency under relative fine grid arrangement. The top boundary of the computational domain is treated as the slip wall. The front and back boundaries are set to the symmetry condition. The ground and the building walls are set as the solid boundaries. The left and right boundaries are set as inlet and outlet.

The mean wind speed profile of the inlet boundary is determined by the Equation (6)

$$U = \frac{u^*}{\kappa} \ln \left(\frac{z-d+z_0}{z_0} \right) \quad (6)$$

where u^* is the friction velocity, κ is the von Karman constant, z is the height coordinate, d is the ground-normal displacement height, z_0 is the aerodynamic roughness length.

The friction velocity can be described by Equation (7)

$$u^* = \frac{U_{\text{ref}} \kappa}{\ln \left(\frac{z_{\text{ref}} + z_0}{z_0} \right)} \quad (7)$$

where the reference wind speed U_{ref} is 4.491 m/s, the reference height $z_{\text{ref}} = h = 60$ m, and the aerodynamic roughness length $z_0 = 1.478$ m. Finally, the friction velocity u^* is estimated to be 0.482 m/s.

The turbulent kinetic energy k is prescribed as

$$k = \frac{(u^*)^2}{\sqrt{C_\mu}} \sqrt{C_1 \ln \left(\frac{z-d+z_0}{z_0} \right) + C_2} \quad (8)$$

and turbulent kinetic energy dissipation rate is

$$\varepsilon = \frac{(u^*)^3}{\kappa(z-d+z_0)} \sqrt{C_1 \ln \left(\frac{z-d+z_0}{z_0} \right) + C_2} \quad (9)$$

where C_μ is the empirical modelling constant, C_1 and C_2 are the curve-fitting coefficients. Similar setting of the boundary conditions can be found in Keshavarzian et al. (2021) as well as OpenFoam (2021).

The CFD simulations are performed on the OpenFOAM platform. The wall function named atmNutmWallFunction in OpenFOAM is applied for the solid wall boundaries. The semi-implicit method for pressure linked equations (SIMPLE) algorithm is used to handle pressure-velocity coupling in incompressible flows. The second-order accurate Gaussian integration and linear schemes are used to calculate the gradient and the divergence terms, respectively. The CFD

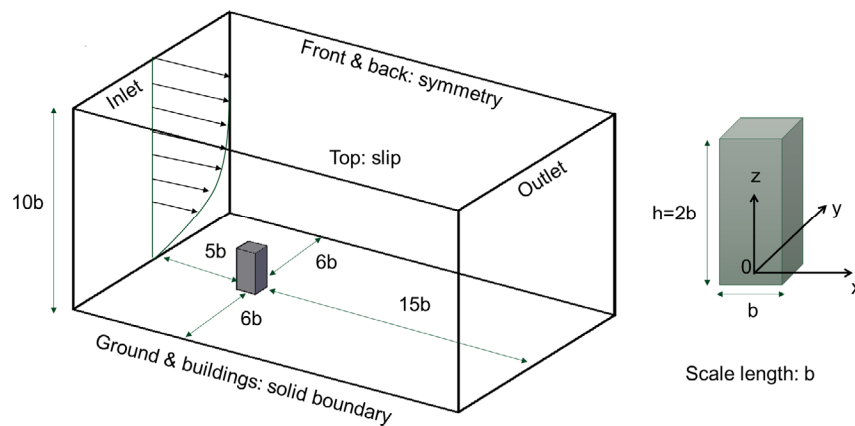


Fig. 3 Schematic of computational domain and building model

simulations are considered to converge when all the residuals of iteration are less than 10^{-6} . We also add the LES simulation with the same computation domain and grid arrangement for base case to compare with the RANS results, following the similar LES framework (Wang et al. 2021a; Wang et al. 2021b). The one-equation subgrid-scale (SGS) model is used to parametrize the SGS stresses. The pressure-implicit with splitting of operators (PISO) algorithm and second-order discretization schemes are employed in the LES simulation. The residual of the iterative solvers is less than 10^{-6} for converged solution.

2.4 Grid sensitivity and model validation

The computational domain is discretized into finite volume (FV) hexahedral cells by the OpenFOAM utilities blockMesh and snappyHexMesh. The total number of grids for coarse, medium and fine grid setting are about 1 million, 5 million and 8 million grids, respectively. A mesh refinement was executed near the building surfaces with minimum grid size of 0.5 m, 0.25m, and 0.1875m, respectively. The grow ratio of the adjacent grids is less than 1.3 (Zhuang et al. 2014; Franke et al. 2011). The grid sensitivity analyses are conducted through comparing the normalized mean wind speed (U/U_{ref}) and the normalized turbulent kinetic energy (k/U_{ref}^2). The results of the three types of grids have a good agreement. The medium grid (~ 5 million grids) shows sufficient resolution for the model simulation in this work.

Apart from the standard $k-\varepsilon$ model, the RNG $k-\varepsilon$, realizable $k-\varepsilon$ turbulence and LES model are also compared (Figure 4). The RNG $k-\varepsilon$ model modifies the turbulent viscosity and then the rotation and rotational flows in the average flow are considered. The RNG $k-\varepsilon$ model also takes the time mean strain rate of the main stream into the consideration in the equation. The dissipation rate ε equation of the realizable $k-\varepsilon$ model is modified (Nie et al. 2009; Andersson et al. 2012). The $k-\omega$ model is not very adequate in simulating wind environment around the bluff body,

so this study does not choose $k-\omega$ model for comparison. The square building with a size of 1:1:2 is tested in this study to compare the accuracy and applicability of these four turbulence models. LES resolves the large-scale motion and parameterizes the small-scale motion, which is deemed to improve the model performance compared with RANS but still limited by its high computational expense (Tominaga and Stathopoulos 2011).

As shown in Figure 4, the normalized mean wind speed (U/U_{ref}) shows good agreements among different turbulence models before ($x = -0.75b$), at the top of ($x = 0$) and after buildings ($x = 0.75b, 1.5b$, and $2b$). The RANS results are comparable with the LES simulations in this study and by Liu and Niu (2016), with coefficient of determination R^2 over 0.98 and root mean square error RMSE less than 0.16. These results suggested that the standard $k-\varepsilon$ model can generate reasonably accurate results for the mean flow in the recirculation region after the building, which will be used in the following CFD simulations of buildings with different building shapes.

Two wind tunnel datasets with the same 1:1:2 square-shaped building model are used to validate our model performance. Details of the wind tunnel setup and data are available and can be referred to Architectural Institute of Japan (AIJ 2007) and Tanaka et al. (2006). The best log-law (Equation (6)) fitting inflow profiles from the wind tunnel experiments is used as the inlet boundary conditions in the CFD models. The inflow reference velocity ($= 4.491$ m/s and 4.2 m/s in AIJ (2007) and Tanaka et al. (2006), respectively), friction velocity u^* ($= 0.482$ m/s and 0.418 m/s), and z_0 ($= 1.478$ m and 1.099 m) are used in the CFD validation cases. Seven profiles at the vertical xz plane and horizontal xy plane of mean streamwise velocity around the buildings at $x = -0.25b, 0, \pm 0.5b, \pm 0.75b, 2b$ are compared between the CFD-RANS models and wind tunnel measurements (Figure 5). The coefficient of determination R^2 is in the range of 0.88–0.99 for vertical and horizontal wind speed profiles and root mean square

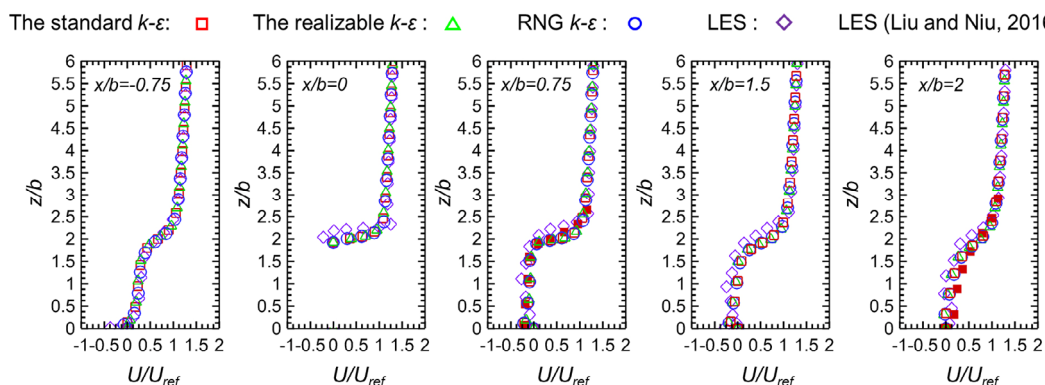


Fig. 4 Comparisons of vertical profiles of the normalized mean wind speed at the vertical center plane of the domain ($y = 0$) among different turbulent models

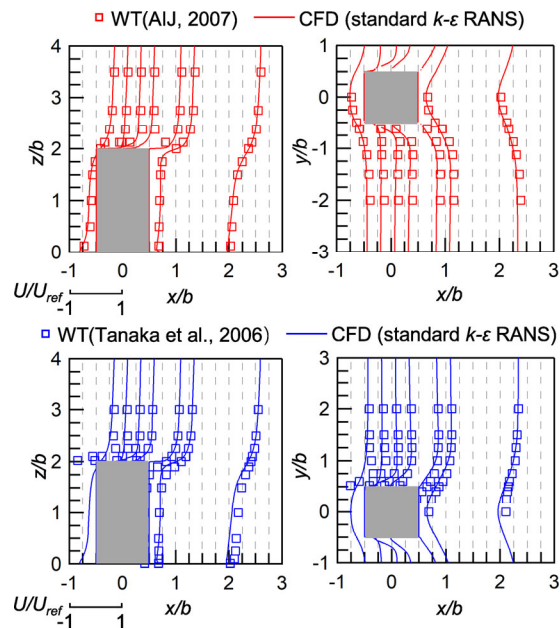


Fig. 5 Profiles of the normalized mean wind speed at the vertical center plane of the domain ($y = 0$) and the horizontal plane ($z = 0.125b$)

error RMSE is 0.10–0.27 so their agreement is favorable, indicating the adequate accuracy of the CFD model for the flow analysis.

3 Results and discussion

3.1 Flow characteristics

3.1.1 Effect of building shapes

Figure 6(a) illustrates the mean flow pattern around the isolated high-rise buildings with eight different cross-section shapes at the pedestrian level (xy plane, $z = 1.75$ m). The vortices symmetrically distributed in the vicinity of these buildings except the L-shaped. There are symmetrical vortices on the leeward side of square, octagon, cross-shaped, #-shaped and H-shaped buildings, while the vortices of triangle and T-shaped buildings are closer to lateral sides of the buildings. There are two additional vortices in the dented structure at the lateral sides of the H-shaped building. In particular, a whole large vortex forms between the two wings of the L-shaped building because of the special cross-section shape.

From the vertical xz plane ($y = 0$) point of view (Figure 6(b)), the vortices are positioned at the upper level of the leeward side ($z > b$). The flow patterns after the square and H-shaped buildings are similar because of the same rectangular leeward surfaces. The dominant vortices are not at the center plane ($y = 0$) for the triangle and T-shaped buildings because of the protrudes. There is

obvious vortex separation behind the #-shaped building because of the close short limbs behind the building. The largest vortex forms on the leeward side of the L-shaped building because of the biggest cavity. It is suggested that the building shapes make a remarkable impact on the size and positions of the vortices.

3.1.2 Building heights

The effects of building height variability are examined for the flows around the square buildings with aspect ratios of $h:b = 2:1, 3:1, 4:1$. As shown in Figure 7(a), two vortices symmetrically distributed on both sides of centerline ($y = 0$), suggesting that no obvious differences are found in the pedestrian-level flow fields behind the buildings with different heights. However, at the vertical xz plane, the vortex will be elevated with increasing building height (Figure 7(b)). In addition, similar size of the vortices at the pedestrian level are found indicating vortex size is mainly governed by the building width rather than height (Tse et al. 2017). Another noticeable feature is that although larger recirculation zone area is observed behind higher buildings at the vertical xz plane, the maximum length of the recirculation zone at the same level of height is comparable, for example $\sim 2b$ at the pedestrian level ($z = 1.75$ m) and $\sim 1.1b$ at $z = b$. It indicates that increasing building height would not significantly affect the lower (e.g. pedestrian) level recirculation zone.

3.1.3 Effect of wind directions

Five typical wind directions including the approaching wind ($\theta = 0^\circ$), the oblique approaching wind ($\theta = 45^\circ$), the lateral approaching wind ($\theta = 90^\circ$), the oblique opposing wind ($\theta = 135^\circ$) and the opposing wind ($\theta = 180^\circ$) are considered to investigate the effect of incident angle on the flow fields around the different shaped buildings.

Due to the symmetrical features of the square, #-shaped building and cross-shaped buildings, the flow fields from the approaching wind ($\theta = 0^\circ$) to the oblique approaching wind ($\theta = 45^\circ$) are shown in Figure 8. The distance between the two vortices on the horizontal xy -plane ($z = 1.75$ m) behind the square building becomes longer and the recirculation zone increases dramatically which is caused by the larger frontal area at $\theta = 45^\circ$ (Fan et al. 2022). On the contrary, the vortices distance and recirculation zone for the #-shaped building and the cross-shaped building decreases as the wind angle θ increases from 0° to 45° mainly because of the dent surface effects. In addition, the notable recirculation vortex forms at the vertical plane behind the square building at $\theta = 45^\circ$, while the vortex becomes smaller for cross-shaped building at $\theta = 45^\circ$ probably attributed to the large cavity of the leeward wall.

There are similar vortices on the xy -plane ($z = 1.75$ m)

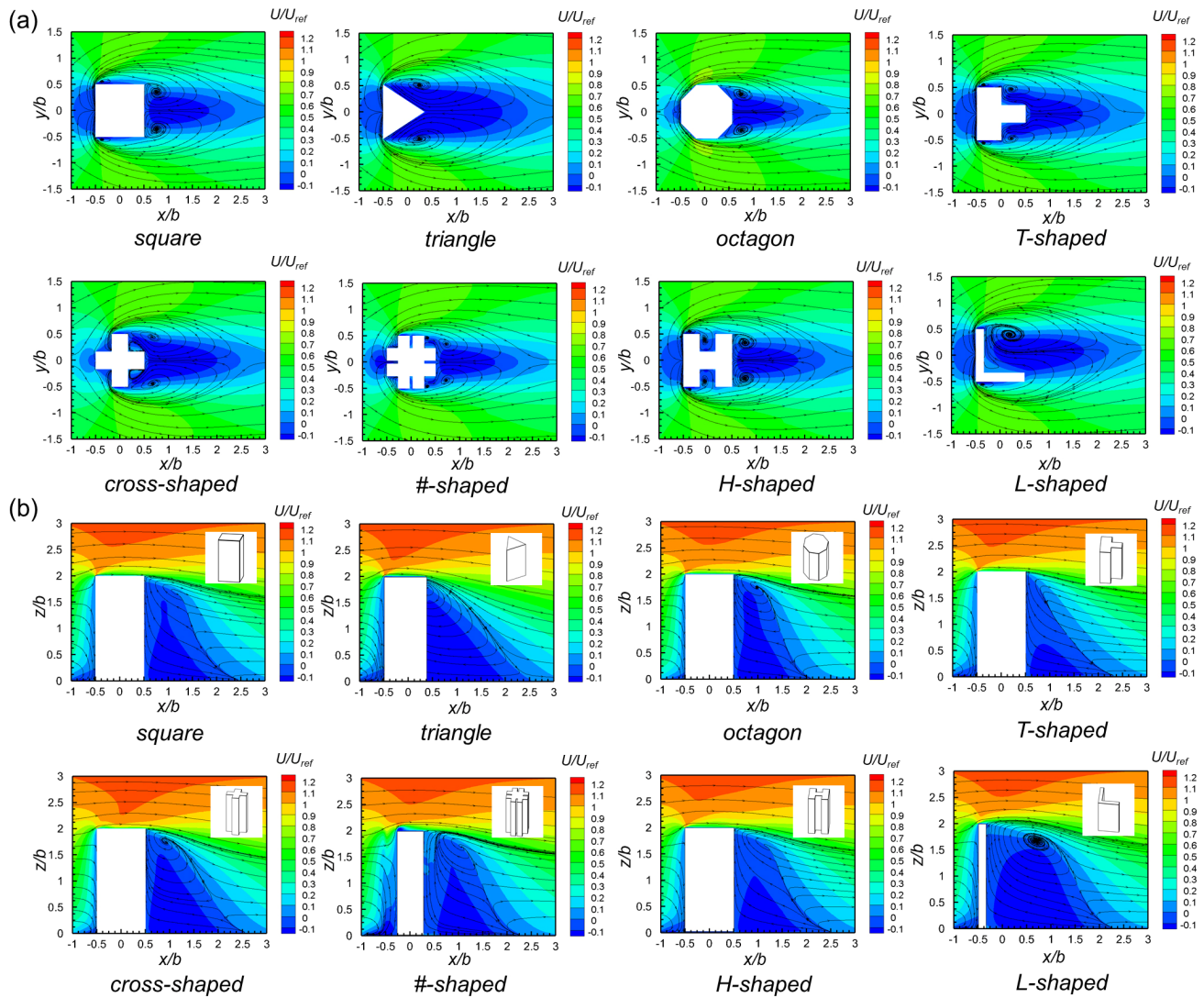


Fig. 6 The normalized mean velocity contours with streamlines of different building shapes on the (a) horizontal xy -plane ($z = 1.75$ m) and (b) vertical xz -plane ($y = 0$)

behind the H-shaped building at $\theta = 0^\circ$ and $\theta = 90^\circ$ (Figure 9). However, the two recirculation vortexes have larger size and longer relative distance at oblique approaching wind ($\theta = 45^\circ$). Meanwhile, on the vertical plane, a distinct vortex is formed on the leeward side of the H-shaped building at $\theta = 45^\circ$. The L-shaped building is the most special among these eight buildings. There is only one single large vortex on the xy -plane ($z = 1.75$ m) when the wind angle is 0° . As the wind direction changes from 45° to 135° , two recirculation vortexes form on the leeward side of the building. The distance between the two vortexes is the largest when the wind direction is 135° . On the vertical xz plane ($y = 0$), there are vortexes between the two wings of the building at $\theta = 45^\circ$, which leads to longer residence time of the flow and hinder the pollutant dispersion.

For the triangle and the T-shaped buildings, the contours of normalized mean velocity and streamlines are shown

with the wind directions of $\theta = 0^\circ, 45^\circ, 90^\circ, 135^\circ$ and 180° in Figure 10. The positions and sizes of the vortexes behind the buildings change constantly with different wind directions. On the horizontal xy plane at pedestrian level ($z = 1.75$ m), the two vortexes are symmetrically distributed on the lateral side of the triangle and T-shaped buildings at the approaching wind ($\theta = 0^\circ$). However, such two vortexes are asymmetrical and the recirculation zone is skewed and become asymmetrical when the wind direction turns to $45^\circ, 90^\circ$ and 135° . The vortexes are ultimately on the leeward side of the building at the opposing wind ($\theta = 180^\circ$). On the vertical xz plane at centerline ($y = 0$), there is a noticeable recirculation vortex behind the triangle building at $\theta = 45^\circ, 90^\circ$ and 180° . The largest one appears at $\theta = 180^\circ$. For the T-shaped building, the noticeable recirculation vortex forms at $\theta = 45^\circ, 90^\circ, 135^\circ$ and 180° but smaller at $\theta = 0^\circ$ probably because of the protruded structure.

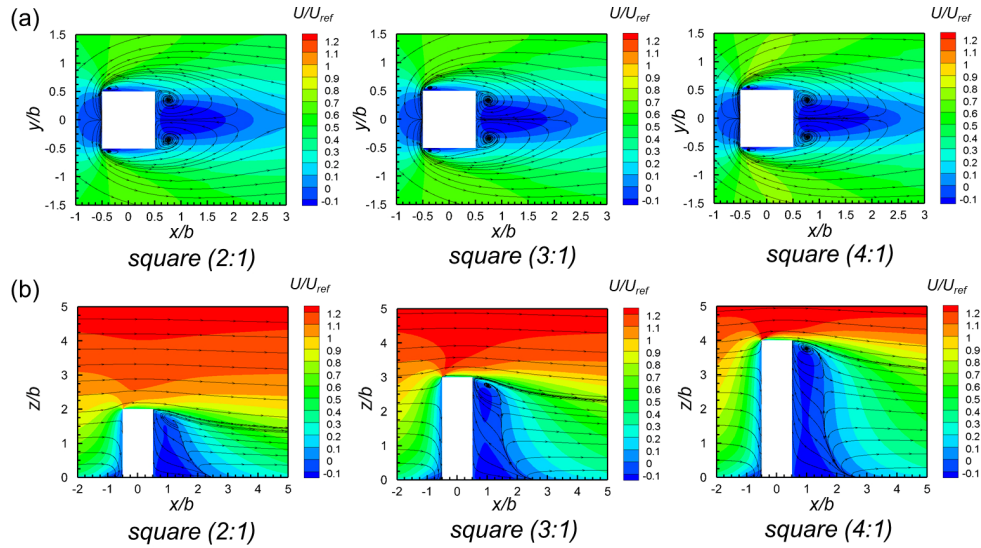


Fig. 7 The normalized mean velocity contours with streamlines of different building-height-to-width ratio ($h/b = 2, 3, 4$) on the (a) horizontal xy -plane ($z = 1.75\text{m}$) and (b) vertical xz -plane ($y = 0$)

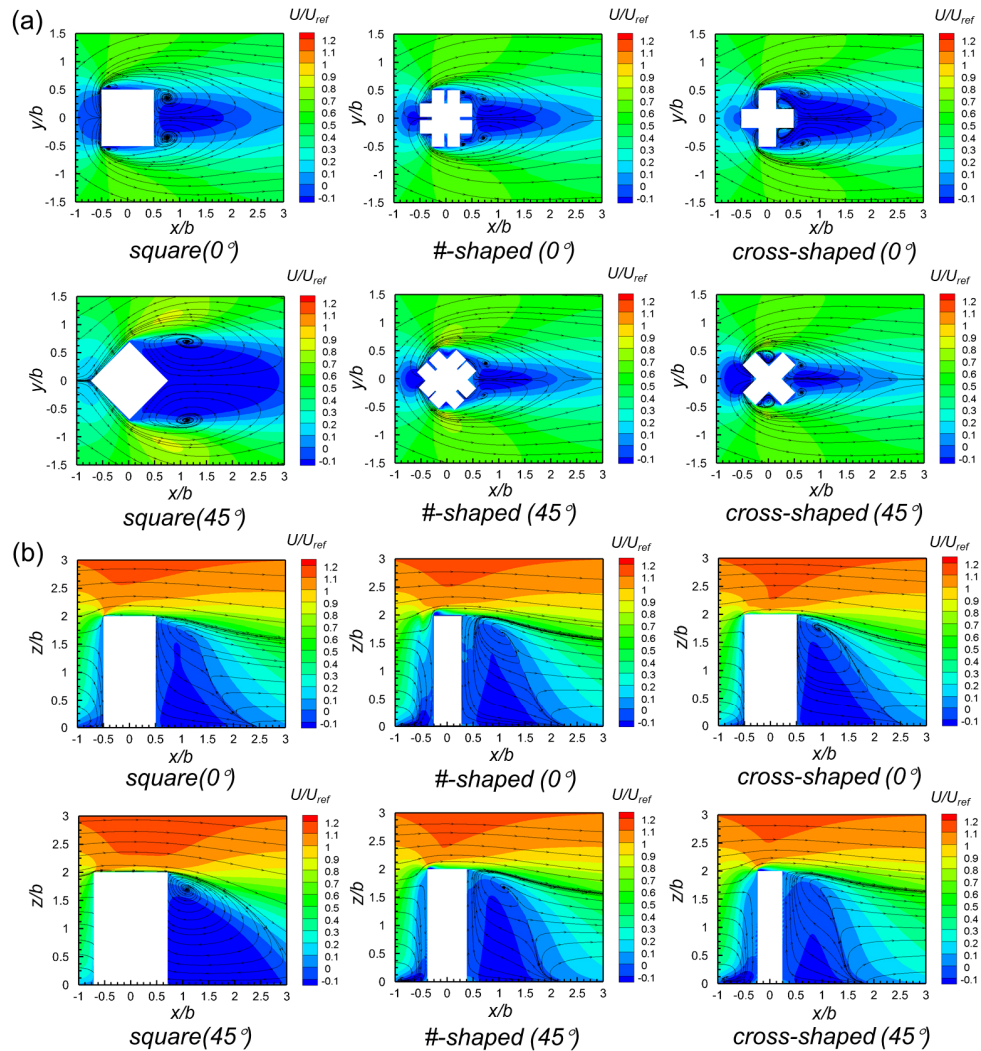


Fig. 8 The normalized mean velocity contours with streamlines of three different building shapes (square, #-shaped, cross-shaped) on the (a) horizontal xy -plane ($z = 1.75\text{m}$) and (b) vertical xz -plane ($y = 0$)

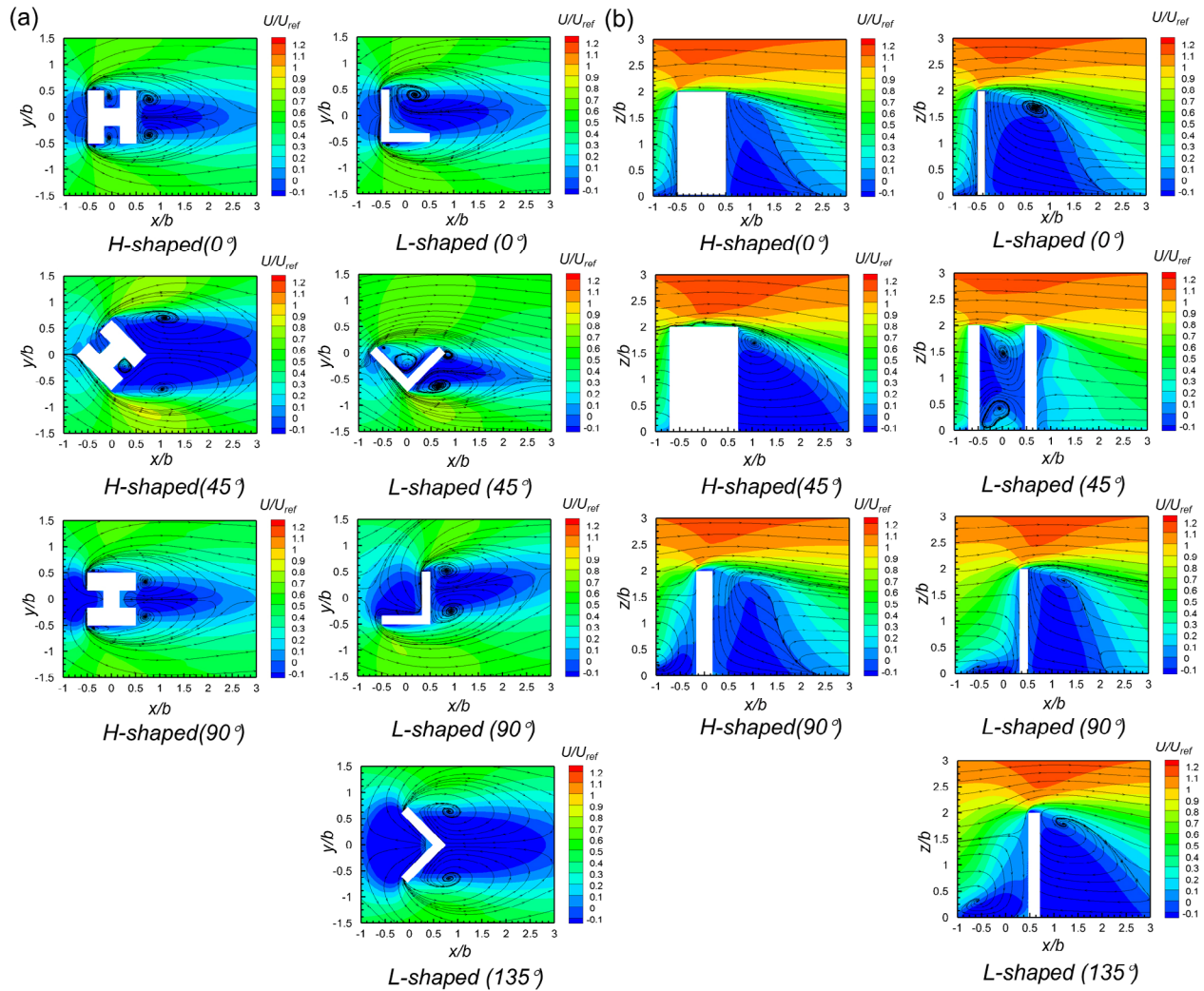


Fig. 9 The normalized mean velocity contours with streamlines of H-shaped and L-shaped buildings on the (a) horizontal xy -plane ($z = 1.75\text{m}$) and (b) vertical xz -plane ($y = 0$)

3.2 Recirculation regions

The recirculation region is where the circulating vortices occur, which in turns significantly affects the ventilation and wind comfort. The recirculation zone area is also used to estimate the drag induced by the building, which is applied to the urban canopy parameterization for the numerical weather and air quality predictions (Belcher et al. 2003; Fan et al. 2022). In this study, the area of the region behind the building, where the normalized mean velocity is less than or equal to 0, is defined as the recirculation area A (Fan et al. 2022). As shown in Figure 11, the area on the vertical xz -plane at the centerline ($y = 0$) is the vertical recirculation area A_v and A_h is the horizontal recirculation area at pedestrian level ($z = 1.75\text{ m}$). The largest streamwise length of this recirculation area is defined as the recirculation length L . The effect of building shapes, building heights and wind directions are examined in the following sections.

Figure 12 illustrates the recirculation length L , vertical recirculation area A_v and horizontal recirculation area A_h behind buildings with different shapes. The recirculation length L behind different buildings are in the range of $1.6b - 2.6b$, with an average of $2b$. The longest distance is found for L-shaped building, reaching about $2.6b$, followed by the triangle building ($L = 2.1b$). The square, cross-shaped, #-shaped and the H-shaped buildings share the similar recirculation length L , which is close to $2b$, followed by the T-shaped building ($L = 1.8b$). The recirculation length L of the octagon building is the smallest ($L = 1.6b$), which is 38% less than the L-shaped building ($L = 2.6b$).

On the vertical plane, the recirculation area A_v of the L-shaped building is the largest ($A_v > 3b^2$), while the T-shaped building has the smallest vertical recirculation area ($A_v = 1.5b^2$), which even less than half of the L-shaped building. The A_v for the square, triangle and H-shaped model is close to $2b^2$, and those A_v of the cross-shaped

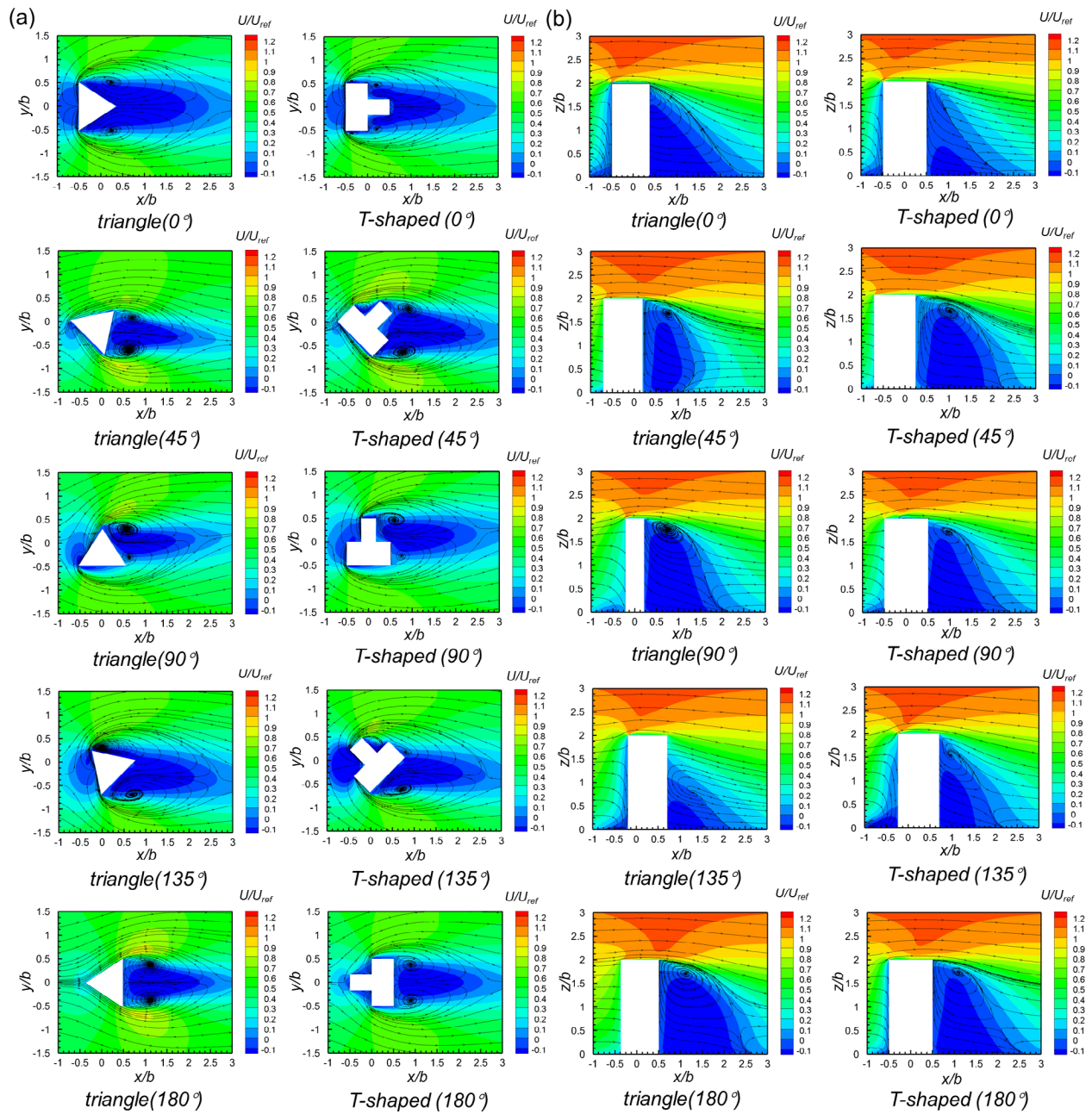


Fig. 10 The normalized mean velocity contours with streamlines of two different building shapes (triangle and T-shaped) on the (a) horizontal xy -plane ($z = 1.75\text{m}$) and (b) vertical xz -plane ($y = 0$)

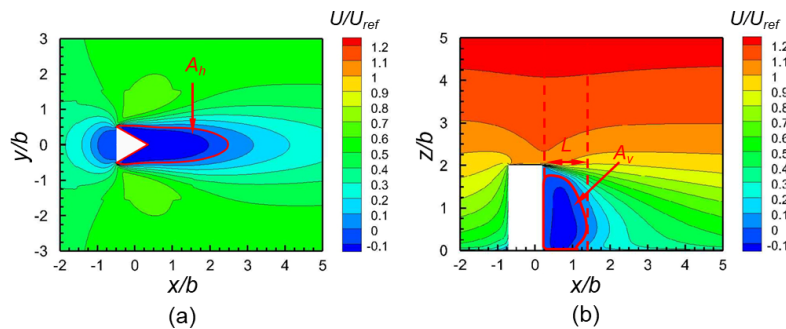


Fig. 11 (a) Horizontal recirculation area A_h at pedestrian level ($z = 1.75\text{ m}$) and (b) the maximum recirculation length (L), vertical recirculation area A_v at centerline ($y = 0$)

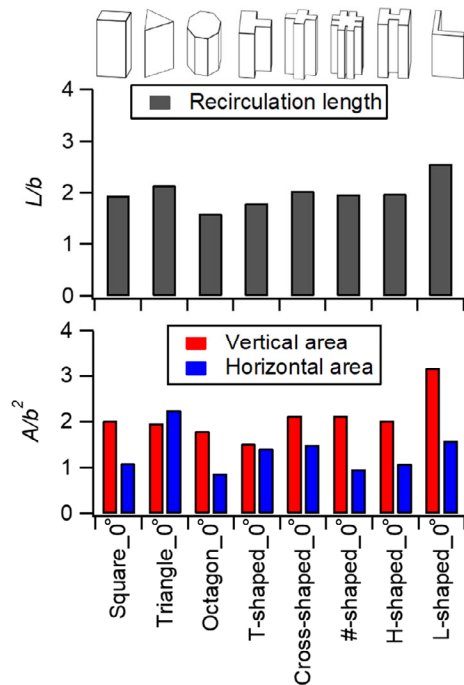


Fig. 12 Effect of building cross-section shapes on recirculation length ($y = 0$), vertical recirculation area ($y = 0$), and horizontal recirculation area ($z = 1.75\text{m}$) after buildings

and #-shaped building have the similar magnitude ($2.1b^2$). On the horizontal plane, there is the maximum recirculation area A_h behind the triangle building, which is more than $2b^2$, while the area on the leeward of the octagon building is the minimum ($A_h = 0.9b^2$). The area after the #-shaped building is also smaller than b^2 . In addition, such magnitude for the horizontal recirculation region after the square building is close to the H-shaped building because of the same windward and leeward area. In general, the vertical area A_v is in the range of $1.5b^2 - 3.2b^2$ and horizontal area A_h in $0.9b^2 - 2.2b^2$.

To illustrate the effect of building height and wind directions, the changes relative to those of the 2:1 building at the approaching wind ($\theta = 0^\circ$) in recirculation length ($(L - L_{0^\circ})/L_{0^\circ}$), horizontal ($(A_h - A_{h0^\circ})/A_{h0^\circ}$), and vertical recirculation areas ($(A_v - A_{v0^\circ})/A_{v0^\circ}$) are shown in Figure 13. It is obvious that the building height has minor influence on the recirculation length and horizontal recirculation areas behind the square building. However, with increasing building height, the vertical recirculation area rises constantly. The A_v of the 4:1 building increase over one-fold compared with that of 2:1 building.

The wind direction effect on the L , A_h , and A_v varied among different shapes. For the triangle shape, the L and A_h decrease by 0.2%–46.2% and 19.4%–57.5%, respectively, when turning to $\theta = 45^\circ$ – 180° . However, the A_v decreases by 15.1% and 54.5% at $\theta = 45^\circ$ and $\theta = 135^\circ$, respectively, while increases by 19.8% and 39.0% at $\theta = 90^\circ$ and $\theta = 180^\circ$,

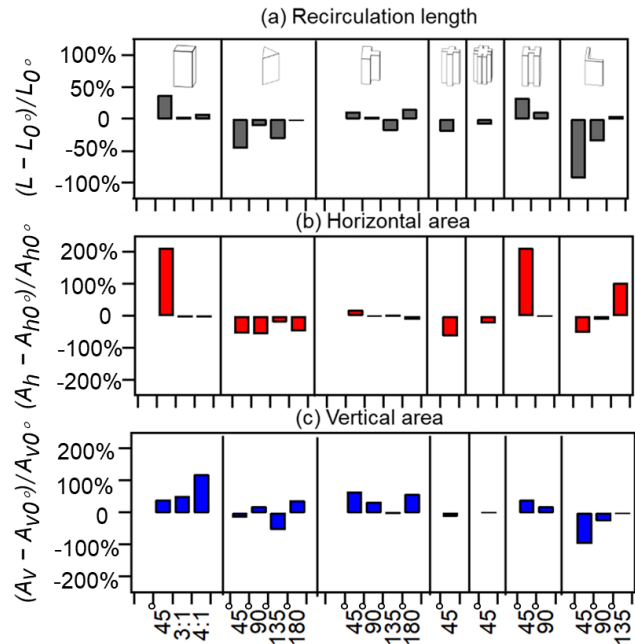


Fig. 13 Effect of wind directions and building heights on recirculation length and recirculation areas after buildings

respectively. Different behaviors were found for the T-shaped building. The L increases by 11.7%, 3.9% and 16.5% at $\theta = 45^\circ$, 90° and 180° , respectively. A_h changes less than 20% between $\theta = 45^\circ$ and 180° . Nevertheless, A_v increases significantly by more than 50% at $\theta = 45^\circ$ and 180° . For the square building, the L , A_h and A_v increase by 37.4%, 212.9% and 41.0%, respectively, due to the frontal area enhancement at the oblique approaching wind ($\theta = 45^\circ$). In contrast, they decrease constantly by 19.8%, 64.6% and 12.2% for the cross-shaped building. For #-shaped building, the wind direction effect is small probably due to the similar surface structure at different approaching wind angles. For the H-shaped buildings, the L and A_v increase by 11.6%–33.2% and 19.1%–40.7%, respectively, as the wind direction changes. A_h increases dramatically by 212.2% at the oblique approaching wind ($\theta = 45^\circ$), but changes less than 1.0% at $\theta = 90^\circ$. The L , A_h and A_v of the L-shaped building change constantly from -92.7% to 5.4% , -53.5% to 102.6% and -97.6% to -4.8% , respectively. In addition, all the value is the largest at $\theta = 135^\circ$ and the least at $\theta = 45^\circ$ because of the block from the two building wings.

3.3 Ventilation assessment

The wind velocity ratio (VR) is widely used as an indication of air ventilation performance. Air ventilation assessment of Hong Kong takes VR as an important parameter in urban climate design (Ng 2009). Xu et al. (2017) used speed-up ratio $R = U_i/U_{i0}$ (where U_i and U_{i0} are the mean wind velocity at point i with and without the building, respectively) to assess

the pedestrian level wind environment. Du and Mak (2017) used the ratio of pedestrian-level mean wind velocity and the reference mean wind velocity (MVR) to evaluate the pedestrian wind comfort supposing the unacceptable wind comfort when the MVR is less than 0.3. However, the wind velocity ratio of most studies was only used to evaluate the ventilation performance of the point by point location, and did not consider the average ventilation performance of a certain area.

In this study, the area-averaged wind velocity ratio (AVR), defined as the ratio of average wind velocity per unit area in the recirculation region, is proposed for the recirculation region as shown in Equation (10):

$$AVR = \left| \frac{U_{avg}}{U_{ref}} \right| \quad (10)$$

where U_{avg} is the area-averaged wind velocity, U_{ref} is the reference velocity. The AVR is therefore used to compare the ventilation efficiency and wind comfort of recirculation area behind the buildings with different shapes. As shown in Figure 14(a), the highest AVR is observed for triangle building, reaching more than 0.13 and followed by the cross-shaped building which is less than 0.09. The third-largest AVR is found behind the L-shaped building, which is about 0.08. The AVR for square, octagon and H-shaped buildings are around 0.07, followed by the T-shaped building which is over 0.06. There is the least AVR for #-shaped building and it is close to 0.05. It is suggested that the pedestrian level ventilation can be enhanced by the triangle building shape design, while reduced behind #-shaped buildings.

The effects of different incident wind directions and building heights on AVR are shown in Figure 14(b). The AVR of the square building changes insignificantly when the building-height-to-width (aspect) ratio $h/b = 2$ increases to $h/b = 3$. The AVR displays an approximately 11.6% decline if the aspect ratio h/b further increases to 4. The reasons are probably because the higher vortex makes less impact on the pedestrian-level area. The AVR of the square and H-shaped buildings enhanced dramatically ($>100\%$) at the oblique approaching wind ($\theta = 45^\circ$) compared with $\theta = 0^\circ$. The change of the wind angle may lead to constant reductions in the AVR for triangle building. The AVR could drop around 32.2% and 40.2% at $\theta = 45^\circ$ and 90° , while $<10\%$ at $\theta = 135^\circ$ and 180° . The AVR of the T-shaped building increases respectively by 86.3%, 31.3%, 55.1%, 47.9% as the wind direction turns from 45° to 180° . The wind direction 45° causes 51.3% decrease on AVR of the cross-shaped building, while the figure for the #-shaped changes slightly about 4.5% at the oblique approaching wind ($\theta = 45^\circ$). The variation of the wind direction may lead to constant increase in the AVR for the L-shaped buildings in the range of 15.7%–98.8%.

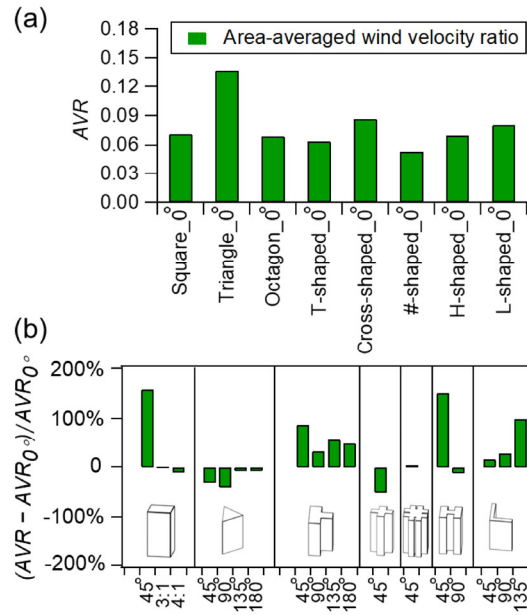


Fig. 14 Effect of wind directions and building heights on area-averaged wind velocity ratio after buildings

3.4 Drag coefficient parameterization

The drag coefficient is an important parameter in the urban canopy model. Its estimation accuracy is strongly affecting the performance of urban climate modeling. Santiago et al. (2007) parameterize C_d for a range of values of frontal area index $\lambda_f (=A_f/A_t$, where A_f is the frontal area of the buildings, A_t is the total floor area), as represented by Equation (11) and denoted as “Scheme_ A_f ”:

$$C_d(z/h) = \begin{cases} 1.2\exp(7.2\lambda_f) & z/h = 0.4 \quad 0.0625 \leq \lambda_f \leq 0.26 \\ 14 - 25\lambda_f & z/h = 0.4 \quad 0.26 < \lambda_f \leq 0.44 \\ 1.7\exp(5.4\lambda_f) & z/h = 0.6 \\ 1.5\exp(4.8\lambda_f) & z/h = 0.8 \end{cases} \quad (11)$$

Later, Santiago and Martilli (2010) proposed another formulation using planar area index $\lambda_p (=A_p/A_t$, where A_p is the building floor area) based on the CFD simulations of $\lambda_p = 0.0625, 0.11, 0.16, 0.25, 0.33, 0.44$, denoted as “Scheme_ A_p ”:

$$C_d = \begin{cases} 3.32\lambda_p^{0.47} & \lambda_p \leq 0.29 \\ 1.85 & \lambda_p > 0.29 \end{cases} \quad (12)$$

As proposed and improved by Taylor (1988) and Fan et al. (2022), the drag parameterization considers the effect of the horizontal recirculation region A_h after the buildings. In this study, we follow their drag model for the isolated buildings:

$$C_d = \frac{C_R A_f}{2[A_t - (A_p + A_h)]} \quad (13)$$

where C_R is the drag constant for an isolated, surface-mounted roughness element. We assume the $A_t = 16b^2$ to estimate the drag over a sparse rough surfaces, in which the recirculation region induced by the building is not affected by the surrounding buildings. As such, this drag model comprehensively considers the influence of A_f , A_p and A_h of the buildings, as denoted as “Scheme_ A_h ”.

Figure 15 shows the drag coefficient normalized by the averaged value ($C_d/C_{d(avg)}$) predicted by the aforementioned parameterization schemes to illustrate the effect of different cross-section building shapes. The drag coefficient estimated by Scheme_ A_f is constant because the λ_f are the same among the buildings with different shapes. For the Scheme_ A_p , the normalized drag coefficient varied in the range of 0.7–1.2, suggesting that the building shape could lead to 50% difference in the drag estimation. As for the Scheme_ A_h used in this study, the normalized drag coefficient changed dramatically with different shapes, ranging from 0.3 for octagon to 1.9 for triangle building. This indicates that building shapes have a significant effect on the drag coefficient estimation, and the consideration of the horizontal recirculation area could refine and improve the drag parameterization for urban canopy model.

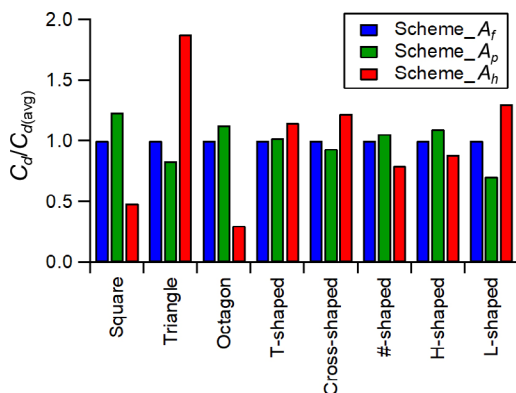


Fig. 15 Effect of building shapes on the ratio of drag coefficient C_d to the average value $C_{d(avg)}$ under different methods

4 Conclusions

This study examines the effects of the building cross-section shape, building height, and wind directions on the flow characteristics, recirculation length, horizontal and vertical recirculation areas behind a high-rise building. We find that the flows behind the square and H-shaped building have similar characteristics including streamlines, the vortex location, recirculation length and area due to the similar rectangular windward and leeward surfaces. On the horizontal plane ($z = 1.75$ m), only a single large vortex forms behind the L-shaped building. The increase of the height does not cause significant influence on the recirculation length and horizontal recirculation area at the pedestrian level ($z =$

1.75 m) behind the square building, but the location of the main vortex is elevated and the recirculation area becomes larger on the vertical xz -plane. The distance between the two vortices on the horizontal xy -plane ($z = 1.75$ m) behind the #-shaped and cross-shaped buildings decreases as the wind direction turns from 0° to 45° . The two vortices behind the triangle and T-shaped buildings become asymmetrical and of different sizes when the wind direction changes.

The recirculation length L after the high-rise buildings with different building shapes are in the range of $1.6b - 2.6b$, with an average of $2b$. There is the longest recirculation length behind L-shaped buildings ($2.6b$) and the shortest behind octagon buildings ($1.6b$). The recirculation vertical area A_v are in the range of $1.5b^2 - 3.2b^2$ and horizontal area A_h in $0.9b^2 - 2.2b^2$, exhibiting about a two-fold difference among different building shapes. It is shown that the L , A_v and A_h generally increase with increasing approaching frontal area when the wind direction changes. Nevertheless, the dent structures of the #-shaped and cross-shaped buildings suppress the recirculation zone. The A_h increases over 200% at $\theta = 45^\circ$ for the square and H-shaped buildings, and the A_v changes less than 50% with different wind incident angles.

The building shape has a great impact on the pedestrian level ventilation in the recirculation zone behind the high-rise building evaluating by the AVR. The AVR is in the range of 0.05 and 0.14, which is around a three-fold difference among the buildings with different building shapes. The largest AVR is found for the triangle building, reaching more than 0.13. The AVR is also significantly affected by the wind direction, especially for the square and H-shaped buildings. It could increase by more than 100% on the AVR at the oblique approaching wind ($\theta = 45^\circ$) compared with the approaching wind ($\theta = 0^\circ$).

The drag parameterization considering the recirculation region shows that the drag coefficient C_d is significantly influenced by the different building shapes, with over 150% variations, suggesting that refining the drag model by accounting the building shape is important in reducing the estimation uncertainty.

The findings of this study provide better understandings of recirculation zone characteristics and pedestrian level ventilation behind the high-rise buildings with different cross-section shapes. It could assist in the urban design and canopy parameterization using the recirculation area as an input variable which has not taken the building shapes into consideration. Currently, no universal parameter for quantifying the building shapes at present, the proportion and number of buildings with different shapes can be considered for fine classification, so as to increase the accuracy of drag coefficient estimation and improve the urban canopy model. As a prior work, this study examines

the recirculation flows after the isolated building, which helps distinguish the effects of building cross-section shapes. However, the flows are more complex around the building clusters, which are highly complicated by the building height, separation and layout. We will perform CFD simulations of building groups and investigate the impact of the high-rise building shapes on flows surrounded by different arrangements of lower buildings in the near future.

Acknowledgements

This work was supported by the National Natural Science Foundation of China – Youth Science Foundation Project No. 42205073, Guangdong Basic and Applied Basic Research Foundation No. 2021A1515110182, Guangdong Natural Science Fund No. 2023A1515012863, and the Innovation Group Project of the Southern Marine Science and Engineering Guangdong Laboratory (Zhuhai) No. 311020001.

Declaration of competing interest

The authors have no competing interests to declare that are relevant to the content of this article.

Author contribution statement

All authors contributed to the study conception and design. Numerical simulation, model validation, visualization and data analysis were performed by Keyi Chen and Ziwei Mo. The first draft of the manuscript was written by Keyi Chen and manuscripts editing was performed by Ziwei Mo and Jian Hang. All authors commented on previous versions of the manuscript. All authors read and approved the final manuscript.

References

- Andersson B, Andersson R, Håkansson L, et al. (2012). *Computational Fluid Dynamics for Engineers*. Cambridge, UK: Cambridge University Press.
- AIJ (2007). *Guidebook for Practical Applications of CFD to Pedestrian Wind Environment around Buildings*. Architectural Institute of Japan.
- Belcher SE, Jerram N, Hunt JCR (2003). Adjustment of a turbulent boundary layer to a canopy of roughness elements. *Journal of Fluid Mechanics*, 488: 369–398.
- Blocken B, Stathopoulos T, van Beeck JPAJ (2016). Pedestrian-level wind conditions around buildings: Review of wind-tunnel and CFD techniques and their accuracy for wind comfort assessment. *Building and Environment*, 100: 50–81.
- Chen L, Mak CM (2021). Numerical evaluation of pedestrian-level wind comfort around “lift-up” buildings with various unconventional configurations. *Building and Environment*, 188: 107429.
- Ding P, Zhou X, Wu H, et al. (2022). An efficient numerical approach for simulating airflows around an isolated building. *Building and Environment*, 210: 108709.
- Du Y, Mak CM (2017). Effect of lift-up design on pedestrian level wind comfort around isolated building under different wind directions. *Procedia Engineering*, 205: 296–301.
- Fan MY, Li WJ, Luo XL, et al. (2022). Parameterised drag model for the underlying surface roughness of buildings in urban wind environment simulation. *Building and Environment*, 209: 108651.
- Franke J, Hellsten A, Schlünzen KH, et al. (2011). The COST 732 Best Practice Guideline for CFD simulation of flows in the urban environment: a summary. *International Journal of Environment and Pollution*, 44: 419.
- Hemida H, Šarkić Glumac A, Vita G, et al. (2020). On the flow over high-rise building for wind energy harvesting: An experimental investigation of wind speed and surface pressure. *Applied Sciences*, 10: 5283.
- Jiang G, Yoshie R (2020). Side ratio effects on flow and pollutant dispersion around an isolated high-rise building in a turbulent boundary layer. *Building and Environment*, 180: 107078.
- Kasana D, Tayal D, Choudhary D, et al. (2022). Evaluation of aerodynamic effects on a tall building with various cross-section shapes having equal area. *Forces in Mechanics*, 9: 100134.
- Keshavarzian E, Jin R, Dong K, et al. (2021). Effect of building cross-section shape on air pollutant dispersion around buildings. *Building and Environment*, 197: 107861.
- Kono T, Kogaki T, Kiwata T (2016). Numerical investigation of wind conditions for roof-mounted wind turbines: effects of wind direction and horizontal aspect ratio of a high-rise cuboid building. *Energies*, 9: 907.
- Korycki M, Łobocki L, Wyszogrodzki A (2016). Numerical simulation of stratified flow around a tall building of a complex shape. *Environmental Fluid Mechanics*, 16: 1143–1171.
- Lee KY, Mak CM (2022). Effects of different wind directions on ventilation of surrounding areas of two generic building configurations in Hong Kong. *Indoor and Built Environment*, 31: 414–434.
- Li Y, Chen L (2020). Study on the influence of voids on high-rise building on the wind environment. *Building Simulation*, 13: 419–438.
- Liu J, Niu J (2016). CFD simulation of the wind environment around an isolated high-rise building: An evaluation of SRANS, LES and DES models. *Building and Environment*, 96: 91–106.
- Liu J, Hui Y, Yang Q, et al. (2021). Flow field investigation for aerodynamic effects of surface mounted ribs on square-sectioned high-rise buildings. *Journal of Wind Engineering and Industrial Aerodynamics*, 211: 104551.
- Meena RK, Raj R, Anbukumar S (2022). Effect of wind load on irregular shape tall buildings having different corner configuration. *Sādhanā*, 47: 126.
- Ng E (2009). Policies and technical guidelines for urban planning of high-density cities - air ventilation assessment (AVA) of Hong Kong. *Building and Environment*, 44: 1478–1488.
- Nie S, Zhou X, Zhou T, et al. (2009). Numerical simulation of 3D atmospheric flow around a bluff body of CAARC standard high-rise

- building model. *Journal of Civil, Architectural & Environmental Engineering*, 31(6): 40–46. (in Chinese)
- OpenFoam (2021). User Guide v2112. Available at <https://www.openfoam.com/documentation/guides/latest/doc/guide-bcs-inlet-atm-atmBoundaryLayer.html>. Assessed 7 Oct 2023.
- Rukhaiyar A, Jayant B, Dahiya K, et al. (2023). CFD simulations for evaluating the wind effects on high-rise buildings having varying cross-sectional shape. *Journal of Structural Fire Engineering*, 14: 285–300.
- Santiago J, Coceal O, Martilli A, et al. (2007). Spatially averaged properties of turbulent flow over staggered arrays of cubes with different packing densities: analysis of the sectional drag coefficients. In: Proceedings of the 7th Symposium on the Urban Environment, San Diego, USA.
- Santiago JL, Martilli A (2010). A dynamic urban canopy parameterization for mesoscale models based on computational fluid dynamics reynolds-averaged navier–stokes microscale simulations. *Boundary-Layer Meteorology*, 137: 417–439.
- Serteser N, Karadag I (2018). Design for improving pedestrian wind comfort: a case study on a courtyard around a tall building. *Architectural Science Review*, 61: 492–499.
- Shao Y, Yang Y (2005). A scheme for drag partition over rough surfaces. *Atmospheric Environment*, 39: 7351–7361.
- Tamura Y, Xu X, Tanaka H, et al. (2017). Aerodynamic and pedestrian-level wind characteristics of super-tall buildings with various configurations. *Procedia Engineering*, 199: 28–37.
- Tanaka H, Yoshie R, Hu C (2006). Uncertainty in measurements of velocity and concentration around a building. In: Proceedings of the 4th International Symposium on Computational Wind Engineering.
- Taylor PA (1988). Turbulent wakes in the atmospheric boundary layer. In: Steffen WL, Denmead OT (eds), *Flow and Transport in the Natural Environment: Advances and Applications*. Berlin: Springer.
- Thordal MS, Bennetsen JC, Koss HHH (2019). Review for practical application of CFD for the determination of wind load on high-rise buildings. *Journal of Wind Engineering and Industrial Aerodynamics*, 186: 155–168.
- Tominaga Y, Stathopoulos T (2011). CFD modeling of pollution dispersion in a street canyon: comparison between LES and RANS. *Journal of Wind Engineering and Industrial Aerodynamics*, 99: 340–348.
- Tominaga Y, Stathopoulos T (2013). CFD simulation of near-field pollutant dispersion in the urban environment: A review of current modeling techniques. *Atmospheric Environment*, 79: 716–730.
- Tominaga Y (2015). Flow around a high-rise building using steady and unsteady RANS CFD: Effect of large-scale fluctuations on the velocity statistics. *Journal of Wind Engineering and Industrial Aerodynamics*, 142: 93–103.
- Tominaga Y, Akabayashi SI, Kitahara T, et al. (2015). Air flow around isolated gable-roof buildings with different roof pitches: Wind tunnel experiments and CFD simulations. *Building and Environment*, 84: 204–213.
- Tse KT, Weerasuriya AU, Zhang X, et al. (2017). Pedestrian-level wind environment around isolated buildings under the influence of twisted wind flows. *Journal of Wind Engineering and Industrial Aerodynamics*, 162: 12–23.
- Vranešević KK, Vita G, Bordas SPA, et al. (2022). Furthering knowledge on the flow pattern around high-rise buildings: LES investigation of the wind energy potential. *Journal of Wind Engineering and Industrial Aerodynamics*, 226: 105029.
- Wang F, Liu CH, Xie J (2021a). Wake dynamics and pollutant dispersion behind a light-duty lorry. *Physics of Fluids*, 33: 095127.
- Wang W, Cao Y, Okaze T (2021b). Comparison of hexahedral, tetrahedral and polyhedral cells for reproducing the wind field around an isolated building by LES. *Building and Environment*, 195: 107717.
- Xu X, Yang Q, Yoshida A, et al. (2017). Characteristics of pedestrian-level wind around super-tall buildings with various configurations. *Journal of Wind Engineering and Industrial Aerodynamics*, 166: 61–73.
- Yang Q, Xu X, Lin Q, et al. (2022). Generic models for predicting pedestrian-level wind around isolated square-section high-rise buildings. *Journal of Wind Engineering and Industrial Aerodynamics*, 220: 104842.
- Yu Y, Kwok KCS, Liu XP, et al. (2017). Air pollutant dispersion around high-rise buildings under different angles of wind incidence. *Journal of Wind Engineering and Industrial Aerodynamics*, 167: 51–61.
- Zhang B, Ooka R, Kikumoto H (2020a). Analysis of turbulent structures around a rectangular prism building model using spectral proper orthogonal decomposition. *Journal of Wind Engineering and Industrial Aerodynamics*, 206: 104213.
- Zhang X, Weerasuriya AU, Lu B, et al. (2020b). Pedestrian-level wind environment near a super-tall building with unconventional configurations in a regular urban area. *Building Simulation*, 13: 439–456.
- Zhang X, Weerasuriya AU, Zhang X, et al. (2020c). Pedestrian wind comfort near a super-tall building with various configurations in an urban-like setting. *Building Simulation*, 13: 1385–1408.
- Zhang B, Ooka R, Kikumoto H (2021). Identification of three-dimensional flow features around a square-section building model via spectral proper orthogonal decomposition. *Physics of Fluids*, 33: 035151.
- Zheng X, Montazeri H, Blocken B (2020). CFD simulations of wind flow and mean surface pressure for buildings with balconies: Comparison of RANS and LES. *Building and Environment*, 173: 106747.
- Zhuang Z, Yu Y, Ye H, et al. (2014). Review on CFD simulation technology of wind environment around buildings. *Building Science*, 30(2): 108–114. (in Chinese)